Sciencexpress Reports

Keeping cool: Enhanced optical reflection and heat dissipation in silver ants

Norman Nan Shi,[1] Cheng-Chia Tsai,[1] Fernando Camino,[2] Gary D. Bernard,[3] Nanfang Yu,[1]* Rüdiger Wehner[4]*

[1]Department of Applied Physics and Applied Mathematics, Columbia University, New York, USA. [2]Center for Functional Nanomaterials, Brookhaven National Laboratory, USA. [3]Department of Electrical Engineering, University of Washington, USA. [4]Brain Research Institute, University of Zürich, Switzerland.

*Corresponding author. E-mail: ny2214@columbia.edu (N.Y.); rwehner@zool.uzh.ch (R.W.)

Saharan silver ants, *Cataglyphis bombycina*, forage under extreme temperature conditions in the African desert. We show that the ants' conspicuous silvery appearance is created by a dense array of uniquely shaped triangular hairs with two thermoregulatory effects. They enhance not only the reflectivity of the ant's body surface in the visible and near-infrared range of the spectrum, where solar radiation culminates, but also the emissivity of the ant in the mid-infrared. The latter effect enables the animals to efficiently dissipate heat back to the surroundings via blackbody radiation under full daylight conditions. This biological solution for a thermoregulatory problem may lead to the development of biomimetic coatings for passive radiative cooling of objects.

The silver ants of the Sahara desert, *Cataglyphis bombycina*, inhabit one of the hottest terrestrial environments on Earth, where they occupy the unique ecological niche of a "thermophilic scavenger" (*1*). In wide-ranging foraging journeys, they search for corpses of insects and other arthropods that have succumbed to the thermally harsh desert conditions, which they themselves are able to withstand more successfully. On hot summer days they reach maximal foraging activities when their body temperatures measured as "operative environmental temperatures" are in the range of 48-51°C (*2*, *3*). In order to survive under these conditions, occasionally the ants must unload excess heat by pausing on top of stones or dry vegetation, where, due to the steep temperature gradient above the sand surface, they encounter considerably lower temperatures. Under the midday sun of a summer day, the ants may resort to this thermal respite (cooling-off) up to 70% of their entire foraging (*3*). In keeping their body temperature below their critical thermal maximum of 53.6°C (*4*), they do not only need to reduce heat absorption from the environment, but also to be able to efficiently dissipate excess heat, so that they can minimize the amount of time spent in thermal refuges.

Here we show, through a series of optical and thermodynamic measurements, full-wave simulations and heat-transfer modeling, how a dense array of uniquely shaped hairs, characteristic for *Cataglyphis bombycina*, enables the ants to maintain lower body temperatures by (i) reflecting a large portion of the solar radiation in the visible and near-infrared (NIR) range of the spectrum, and (ii) radiating heat to the surrounding environment by enhancing the emissivity in the mid-infrared (MIR), where the blackbody radiation spectrum of the ant's body culminates. The thermoregulatory solutions, which the silver ants have evolved to cope with thermally stressful conditions, provide a first example that an animal is able to control electromagnetic waves over an extremely broad range of the electromagnetic spectrum (from the visible to the MIR).

Specimens of *Cataglyphis bombycina* collected in Tunisia (34°10'N, 08°18'E) were used for all the optical and thermodynamic measurements. In these ants, the dorsal and lateral sides of the body have a silvery glare (Fig. 1A), and are covered by dense and uniform arrays of hairs (Fig. 1B and fig. S4). As scanning electron microscopy (SEM) images show, the hairs, which gradually taper off at the tip, are locally aligned in the same direction (Fig. 1C). Their most remarkable structural feature is the triangular cross-section characterized by two corrugated top facets and a flat bottom facet facing the ant's body (Fig. 1, D and E). Cross sectional views obtained by focused ion beam (FIB) milling show that the gap between the bottom hair facet and the cuticular surface also varies but is generally larger than a few hundred nanometers.

Optical reflectivity measurements of ant specimens were obtained with two Fourier transform spectrometers. The visible and NIR measurements showed that hemispherical reflection, i.e., the sum of specular and diffuse reflection collected through an integrating sphere (*2*), is substantially enhanced in regions with intact hair coverage as compared to regions from which the hairs had been removed (Fig. 2A and fig. S1). The hair-covered region reflects 67% of the incoming solar radiation rather than only 41% as is the case after their removal. This enhancement is due to scattering within the triangular hairs (Mie scattering), where light gets trapped and then reradiates out in all directions (*5*–*7*). Individual hairs of given cross-sectional dimensions generate enhanced reflection due to scattering at specific wavelengths where fundamental and higher-order Mie resonance modes are supported (Fig. 2C) (fig. S5). Due to the variation in cross sectional areas, resonance peaks from individual hairs are averaged out, so that the hair cover effectively acts as a broadband reflection enhancement coating.

Due to the ellipsoidal shape of the ant's body, a large

portion of the dorsolateral surface is hit by solar radiation obliquely (fig. S4). This prompted us to examine the reflectivity as a function of the incidence angle of radiation, which was varied from 0° to 80°, with 0° representing the direction normal to the surface. As the results show, Mie scattering enhances reflectivity over all angles when regions with intact hair cover are compared to those with hairs removed (Fig. 2B). With increasing angle of incidence, reflectivity enhancement becomes particularly strong at beyond 30°. This is the critical angle at which total internal reflection starts to occur at the bottom facets of the hairs (Fig. 2D, II). At angles approaching 90°, reflectivity drops off when total internal reflection at one of the top facets starts to direct more of the radiation toward the ant's body (Fig. 2D, III).

Next, we performed finite-difference time-domain (FDTD) simulations, in order to demonstrate the functional significance of the triangular cross-section of the hairs in enhancing reflectivity in the visible and NIR range (figs. S6 to S8). These simulations compared the reflective properties of triangular and circular hairs of the same cross-sectional area. Even though the enhancement of reflectivity at normal incidence is comparable in both cases, triangular hairs produce an extra enhancement at higher angles of incidence (Fig. 2B). The reason is that although Mie scattering of similar strength occurs in both circular and triangular hairs, in the latter the total internal reflection at the bottom facets of the hairs enhances reflectivity substantially further. The high reflectivity disappeared when the specimens were wetted by an ethanol-water solution (fig. S3), which removed the refractive index contrast between air and hairs, and thus destroyed the conditions required for Mie scattering and total internal reflection.

Reflectivity measurements performed in the MIR range revealed a second important point in the silver ant thermotolerance story. When proceeding from lower to higher wavelengths, at about 8 μm, the enhanced reflectivity of regions with hair cover as compared to those without hairs reverses to reduced reflectivity (Fig. 2E). As Kirchhoff's law of thermal radiation states, reduced reflectivity corresponds to enhanced emissivity (*8*). At a body temperature of 50°C, which the silver ants may reach when foraging at peak activity times, the blackbody radiation of the ant's surface would lie in the range of 6 - 16 μm (peaked at ~9 μm) and thus allow the silver ants to offload heat more efficiently through radiative heat transfer. The latter decreases the steady-state body temperature and reduces the respite time.

How does the hair cover with its enhanced reflectivity in the visible and NIR and its enhanced emissivity in the MIR affect the radiative heat transfer between the ant's body and the environment? To investigate this question we performed thermodynamic experiments, which mimicked all radiative heat transfer effects in the silver ants' natural foraging environment (fig. S2). To accomplish this task, we used a high-power xenon lamp to simulate the solar spectral distribution at the desert sand surface (*9*), and a thermoelectrically cooled high-emissivity metal plate to simulate the clear sky with its low level of blackbody radiation (*10*). The ant specimens were suspended on thin threads to minimize thermal conduction. Thermodynamic experiments were conducted in vacuum to study thermal radiation as well as in still air to study the interplay of thermal radiation and convection. Under both conditions the specimens provided with their natural hair covers were able to maintain significantly lower steady-state body temperatures than the same specimens with the hairs removed (Fig. 3).

The thermodynamic experiments conducted in vacuum comparing specimens before and after hair removal further revealed that the hair cover decreases the time constants of temperature change (Fig. 3, B and E). The shortened time constants indicate an increased rate of radiative heat transfer and are a direct confirmation of the effect of the hairs in enhancing the MIR emissivity. By using the time constants and the heat transfer model, we computed that the hair cover enhances emissivity by about 15% (table S1). This enhanced emissivity is due to the fact that at large MIR wavelengths, i.e., at wavelengths much larger than the dimensions of the cross-sections of the hairs, the hair structure acts as a gradient refractive index layer (fig. S9) (*11*–*13*), which provides the surface with broadband, broad-angle antireflective properties in the MIR (Fig. 2, E and F). Due to the influence of convection, the time constants of temperature change decreased by a factor of about three when the specimens were brought from vacuum into air (Fig. 3). This indicates that radiative heat dissipation still played a significant role in the presence of natural convection. It amounted to about one half of convection.

Applying experimentally extracted parameters to the heat transfer model revealed that the enhanced visible and NIR reflectivity and enhanced MIR emissivity have comparable contributions to reducing the steady-state temperature in the presence of natural convection (figs. S10 and S11). On hot summer days in the Sahara, foraging activities of silver ants regularly occur under low wind or even still air conditions, when the ants have to rely on enhanced visible and NIR reflectivity and enhanced MIR emissivity equally heavily to reduce their body temperature during the respite behavior.

It is interesting to note that the hairs cover only the top and the sides of the ant's body, where they are responsible for the effects described above. The absence of hairs on the bottom surface reduces the radiative energy transfer between the hot sand and the cooler ant body, so that the animals can reduce the absorption of blackbody radiation from the desert floor.

In conclusion, Saharan silver ants are covered with a dense array of uniquely shaped triangular hairs on the top and the sides of their bodies. These silvery hairs protect the ants against getting overheated in at least three ways. First, as a result of Mie scattering and total internal reflection the

hairs enhance reflectivity in the visible and near-infrared, where solar radiation culminates. Second, in the mid-infrared, where solar radiation becomes negligible for $\lambda > 2.5\ \mu m$, the hairs acting as an antireflection layer enhance emissivity and thus increase the ants' ability to offload excess heat via blackbody radiation. Third, the ant's bare bottom surface reflects mid-infrared radiation from the hot desert floor more efficiently than if it were covered by hairs. Taken together, these effects result in decreasing the ant's steady-state body temperature and thus enable these thermophilic scavengers to forage at exceedingly high environmental temperatures. Finally, the present interdisciplinary account on the silver ants could have a significant technological impact by inspiring the development of biomimetic coatings for passive cooling of objects (*14*–*16*). Interestingly, a recent article reported the demonstration of a multilayered film that can cool down an object by using essentially the same mechanisms as the silver ants, i.e., high reflectivity in the solar spectrum and high emissivity in the mid-infrared (*17*).

REFERENCES AND NOTES

1. R. Wehner, S. Wehner, Parallel evolution of thermophilia: daily and seasonal foraging patterns of heat-adapted desert ants: *Cataglyphis* and *Ocymyrmex* species. *Physiol. Entomol.* **36**, 271–281 (2011). doi:10.1111/j.1365-3032.2011.00795.x
2. Materials and methods are available as supplementary materials on *Science* Online.
3. R. Wehner, A. C. Marsh, S. Wehner, Desert ants on a thermal tightrope. *Nature* **357**, 586–587 (1992). doi:10.1038/357586a0
4. W. J. Gehring, R. Wehner, Heat shock protein synthesis and thermotolerance in *Cataglyphis*, an ant from the Sahara desert. *Proc. Natl. Acad. Sci. U.S.A.* **92**, 2994–2998 (1995). Medline doi:10.1073/pnas.92.7.2994
5. C. F. Bohren, D. R. Huffman, *Absorption and Scattering of Light by Small Particles* (John Wiley & Sons, 1998).
6. J. Schuller, T. Taubner, M. L. Brongersma, Optical antenna thermal emitters. *Nat. Photonics* **3**, 658–661 (2009). doi:10.1038/nphoton.2009.188
7. D. Lin, P. Fan, E. Hasman, M. L. Brongersma, Dielectric gradient metasurface optical elements. *Science* **345**, 298–302 (2014). Medline doi:10.1126/science.1253213
8. J. R. Howell, R. Siegel, M. P. Mengüç, *Thermal Radiation Heat Transfer* (CRC Press, ed. 5, 2010).
9. K. L. Coulson, *Solar and Terrestrial Radiation: Methods and Measurements* (Academic Press, 1975).
10. J. Monteith, M. Unsworth, *Principles of Environmental Physics* (Academic Press, Oxford, ed. 3, 2007).
11. C.-H. Sun, P. Jiang, B. Jiang, Broadband moth-eye antireflection coatings on silicon. *Appl. Phys. Lett.* **92**, 061112 (2008). doi:10.1063/1.2870080
12. J.-Q. Xi, M. F. Schubert, J. K. Kim, E. F. Schubert, M. Chen, S.-Y. Lin, W. Liu, J. A. Smart, *Nat. Photonics* **1**, 176 (2007).
13. M. J. Minot, Single-layer, gradient refractive index antireflection films effective from 035 to 25 μ. *J. Opt. Soc. Am.* **66**, 515 (1976). doi:10.1364/JOSA.66.000515
14. C. G. Granqvist, A. Hjortsberg, Surfaces for radiative cooling: Silicon monoxide films on aluminum. *Appl. Phys. Lett.* **36**, 139 (1980). doi:10.1063/1.91406
15. P. Berdahl, Radiative cooling with MgO and/or LiF layers. *Appl. Opt.* **23**, 370 (1984). Medline doi:10.1364/AO.23.000370
16. E. Rephaeli, A. Raman, S. Fan, Ultrabroadband photonic structures to achieve high-performance daytime radiative cooling. *Nano Lett.* **13**, 1457–1461 (2013). Medline
17. A. P. Raman, M. A. Anoma, L. Zhu, E. Rephaeli, S. Fan, Passive radiative cooling below ambient air temperature under direct sunlight. *Nature* **515**, 540–544 (2014). Medline doi:10.1038/nature13883
18. R. Wehner, *Jahrb. Akad. Wiss. Lit. Mainz* **89**, 101 (1989).
19. B. Heinrich, *The Hot-Blooded Insects: Strategies and Mechanisms of Thermoregulation* (Harvard Univ. Press, 1993).
20. G. S. Bakken, D. M. Gates, *Heat-Transfer Analysis of Animals: Some Implications for Field Ecology, Physiology, and Evolution* (Perspectives of Biophysical Ecology, Ecological Studies Volume 12, Springer, 1975), pp. 255–290.
21. A. C. Marsh, *Physiol. Zool.* **58**, 629 (1985).
22. H. Heatwole, S. Harrington, *J. Arid Environ.* **16**, 69 (1989).
23. J. M. Chalmers, P. R. Griffiths, *Handbook of Vibrational Spectroscopy* (John Wiley & Sons, 2002).
24. D. H. Raguin, G. M. Morris, Analysis of antireflection-structured surfaces with continuous one-dimensional surface profiles. *Appl. Opt.* **32**, 2582–2598 (1993). Medline doi:10.1364/AO.32.002582
25. D. M. Gates, *Biophysical Ecology* (Dover Publications, 1980).
26. R. A. A. Muzarelli, *Chitin* (Pergamon Press, 1977).
27. S. Sommer, R. Wehner, Leg allometry in ants: Extreme long-leggedness in thermophilic species. *Arthropod Struct. Dev.* **41**, 71–77 (2012). Medline doi:10.1016/j.asd.2011.08.002
28. O. G. Martynenko, P. P. Khramtsov, *Free-Convective Heat Transfer* (Springer, 2005).
29. H. J. Merk, J. A. Prins, *Appl. Sci. Res.* **A4**, 207 (1954).

ACKNOWLEDGMENTS

We acknowledge intriguing discussions with N. Pierce; help with experiments from Z. Li, M.-H. Kim, B. Patterson, and M. Y. Sfeir; and R. F. Foelix for kindly preparing and providing Fig. 1B. The work was supported by the National Science Foundation (PHY-1411445, ECCS-1307948) and the AFOSR MURI program (FA9550-14-1-0389). Research was carried out in part at the Center for Functional Nanomaterials, Brookhaven National Laboratory, which is supported by the U.S. Department of Energy, Office of Basic Energy Sciences, under contract no. DE-SC0012704. Data reported in this paper are archived at http://datadryad.org/resource/doi:10.5061/dryad.2bm50. Author contributions are as follows: R.W. and G.D.B. initiated the study, N.S. and N.Y. designed the study and conducted the analyses, and all authors contributed to developing the study and to drafting the manuscript.

SUPPLEMENTARY MATERIALS

www.sciencemag.org/cgi/content/full/science.aab3564/DC1
Materials and Methods
Supplementary Text
Figs. S1 to S11
References (*19*–*29*)
Movie S1

15 April 2015; accepted 11 June 2015
Published online 18 June 2015
10.1126/science.aab3564

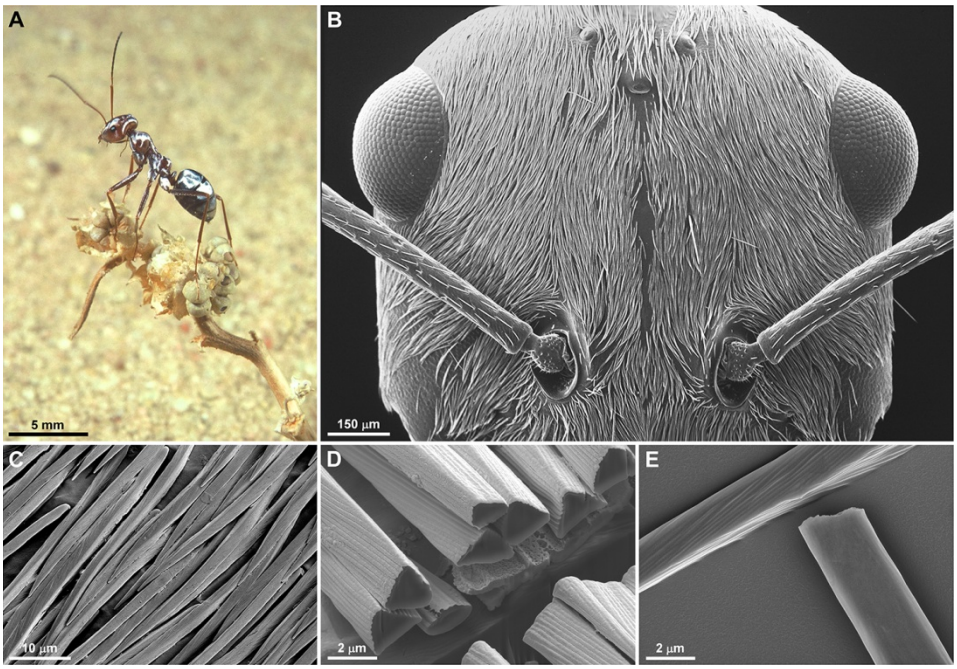

Fig. 1. The bright glare of the silver ant and its structural basis. (**A**) Silver ant offloading heat on top of dry vegetation (*18*). (**B**) SEM frontal view of the head densely covered by hairs. (**C**) SEM image of the hairs gradually tapering off toward the tip. (**D**) Cross-sectional view of the hairs milled with FIB. (**E**) SEM image of two hairs with one flipped upside down to exhibit the flat bottom facet.

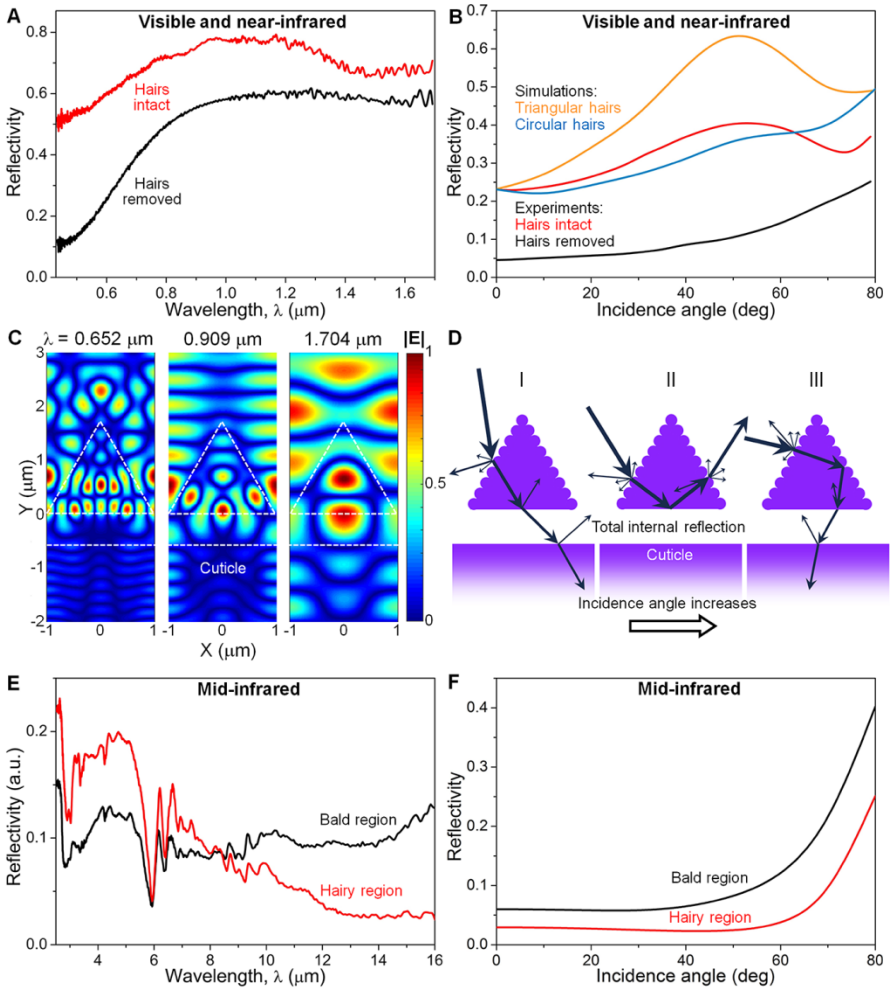

Fig. 2. Reflectivity of the silver ant's body surface from the visible to the mid-infrared range of the spectrum. (**A**) Hemispherical reflectivity measured in the visible and near-infrared. (**B**) Measurement and simulation results showing visible and near-infrared reflectivity as a function of incidence angle. (**C**) Cross-sectional view of two-dimensional distribution of light field (magnitude of electric field component of light, or |E|) around a triangular hair for three exemplary Mie resonances. (**D**) Schematic diagram showing the interaction between visible and near-infrared light and a hair at small (I), intermediate (II), and large (III) incidence angles. The corrugated upper two facets may enhance diffuse reflection in the ultraviolet and visible range. (**E**) Reflectivity measured in the mid-infrared at normal incidence. (**F**) Simulated mid-infrared reflectivity as a function of incidence angle.

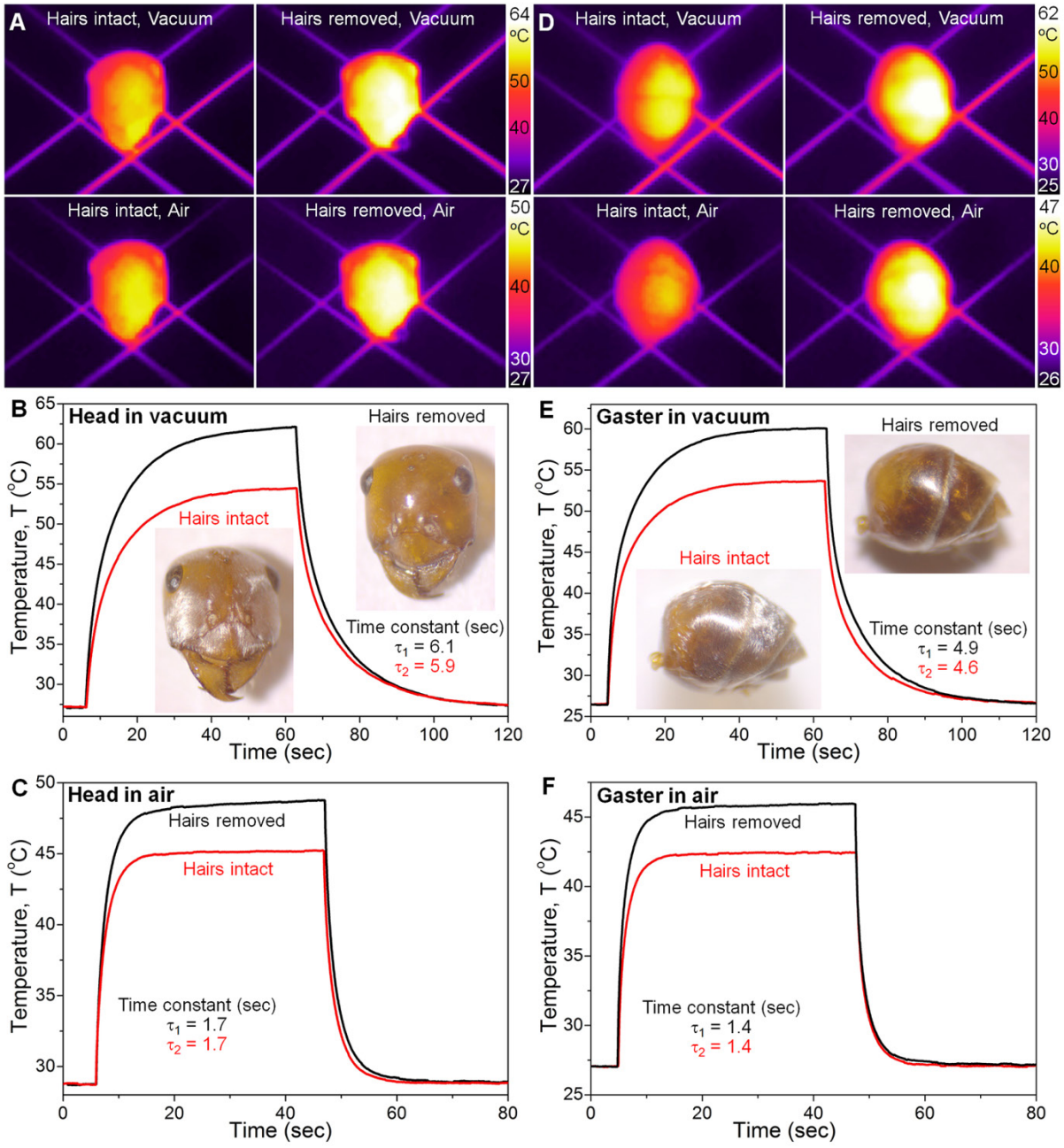

Fig. 3. Results of thermodynamic experiments. (**A**) Thermal camera images showing the head of an ant specimen at thermal steady-state under different conditions. Temporal temperature profiles measured for the head before and after hair removal in vacuum (**B**) and in still air (**C**). (**D** to **F**) Results obtained for the hind part (gaster) of an ant specimen. Insets in (B) and (E) are photos of specimens before and after hair removal. In the "hairs intact" pictures of head and gaster, due to the limited solid angle of illumination, the silvery glance is not shown all over the body surface portrayed in the figures.

www.sciencemag.org/cgi/content/full/science.aab3564/DC1

Supplementary Materials for

Keeping cool: Enhanced optical reflection and heat dissipation in silver ants

Norman Nan Shi, Cheng-Chia Tsai, Fernando Camino, Gary D. Bernard, Nanfang Yu,* Rüdiger Wehner*

*Corresponding author. E-mail: ny2214@columbia.edu (N.Y.); rwehner@zool.uzh.ch (R.W.)

Published 18 June 2015 on *Science* Express
DOI: 10.1126/science.aab3564

This PDF file includes:

Other Supplementary Materials for this manuscript include the following:
(available at www.sciencemag.org/cgi/content/full/science.aab3564/DC1)

Materials and Methods

1. Measurement of silver ants' body temperature

Rather than using the "grab-and-stab" method (capturing the animal, quickly inserting a thermocouple into its body, and reading out the temperature on a digital device), which is difficult to employ satisfactorily due to the ant's small body mass (a few milligrams) and small time constant of temperature change (a few seconds), we measured the "operative environmental temperature" T_e, which is defined as the steady-state temperature attained by the animal in its microenvironment (*19-21*). T_e is an integrative measure of all heat gains and losses due to physical (conductive, convective, and radiative) thermal exchanges between animal and environment - provided that neither metabolic heat production nor evaporative heat losses occur. We measured it by mounting a freshly killed ant (or an equivalent model of it) on the tip of a copper-constantan thermocouple and exposing this probe at ant height to the very environmental condition at which the ants foraged in the field. On summer days, foraging activity started on our Saharan study site at T_e = 46.8°C, and easily rose to 51°C when respite behavior became significant (*3*). In the laboratory, *C. bombycina* has been shown to survive body temperatures of 50.0°C for at least 10.0 +/- 1.3 min (*22*).

The respite effect is enhanced by the behavior of the ants to make efficient use of the micro-topography of the desert surface as well as by the fact that wind speed and turbulence vary both spatially and temporarily above the desert floor, so that convective cooling comes into play at different places in different ways. As the hair cover reduces the ant's steady-state body temperature, the ant having descended from its respite site can increase its foraging time before jumping on the next micro peak to respite again. For a thermographic demonstration of the thermal mosaic on the desert floor, see Fig. 6 in (*1*).

2. Focused ion beam milling and removal of ants' hairs

The cross sectional image (Fig. 1D) was obtained with a focused ion beam/scanning electron microscopy dual system (FEI Helios NanoLab DualBeam). Ion beam at 30 kV and 460 pA was used during the milling process to cut through the hair structure.

The hairs of the ants were removed by gently rubbing a blunt tungsten needle along the skin of the ants. The hairs break easily from their sockets and electrostatically attach to the needle. There is no loss of cuticular material from the ant specimens and all material loss (<1%) is due to the removal of the hairs.

3. Reflectivity measurement

3.1 Reflectivity measurement at normal incidence angle in the visible and near-infrared

For the visible and near-infrared (NIR) portion of the spectrum, reflectivity was captured using a Fourier-transform based spectrometer (Bruker vertex 80) equipped with a laser stabilized high brightness Xenon plasma light source (Energetiq eq-99). The light was focused to a beam spot of ~200 μm in diameter with a plano-convex Calcium Fluoride lens (f=40mm). The reflected light,

including specular and diffuse reflection, was collected with a visible/NIR integrating sphere (Thorlabs IS200-4), coupled with a set of built-in Silicon (Si) and Indium Gallium Arsenide (InGaAs) detectors (*23*). The detected signal was then amplified and fed back into the spectrometer. The hemispherical reflectivity measured has a spectrum range from 0.43 to 1.68 μm.

In order to account for the effective reflectivity of the ant body with respect to the solar spectrum, we defined reflectivity normalized to solar irradiance as:

$$R_{solar} = \frac{\int_{\lambda_1}^{\lambda_2} R(\lambda)M(\lambda)d\lambda}{\int_{\lambda_1}^{\lambda_2} M(\lambda)d\lambda} \quad , \tag{1}$$

where λ_1 and λ_2 are the two ends of the spectrum measured by our visible/NIR Fourier transform spectrometer. $R(\lambda)$ is the hemispherical reflectivity as a function of wavelength, and $M(\lambda)$ is the solar spectral irradiance profile as a function of wavelength, estimated here by assuming perfect blackbody radiation from the sun, with T ~ 5800 K. The obtained value R_{solar} characterizes the overall percentage of power of light reflected by the specimen assuming that the incoming radiation matches the solar spectrum.

3.2 Polarization dependence of the reflectivity spectra in the visible and near-infrared

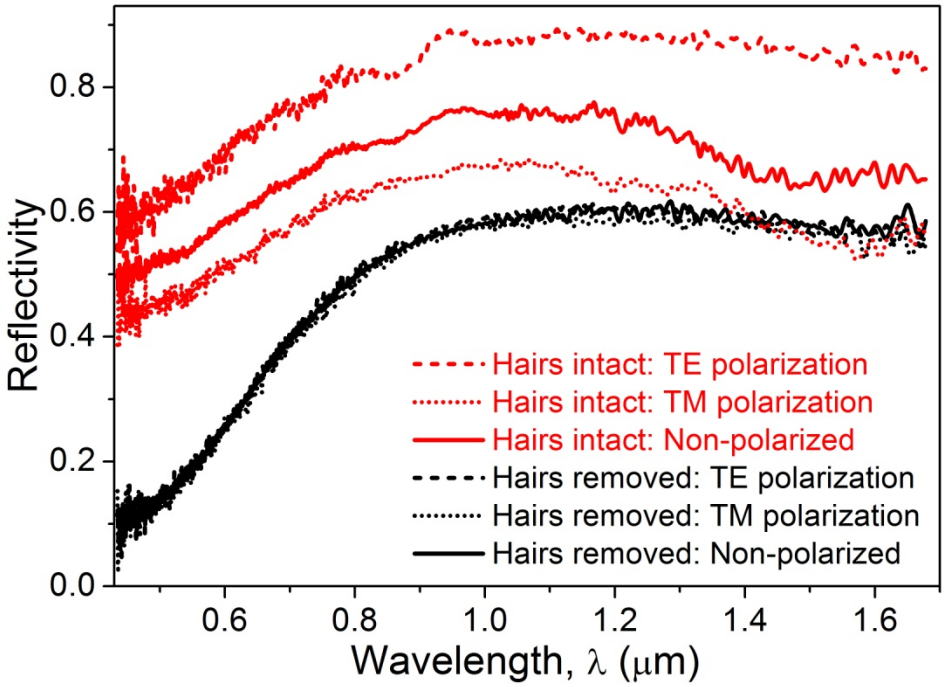

Fig. S1 Reflectivity spectra obtained using transverse-electric (TE), transverse-magnetic (TM), and unpolarized light produced by a Xenon lamp. The TE (TM) polarization is defined as the situation in which the electric field component of the incident light is parallel (perpendicular) to the orientation of the hair array. Polarized light was created by inserting a

broadband wire-grid polarizer into the beam path, at a location before light was focused onto the specimens. Spectra for unpolarized incident radiation (also shown in Fig. 2A) were obtained by removing the polarizer.

As shown in Fig. S1, The hair array acts as a birefringent layer, where higher reflectivity was observed for TE polarized light when compared to TM polarized light. When the hairs have been removed, there is no difference in the spectra obtained with TE, TM, and unpolarized light. The high reflectivity in the NIR is partially due to the internal microstructures of the cuticle itself (not the focus of the present study).

3.3 Angular reflectivity measurement in the visible and near-infrared

The reflectivity of specimens was measured as a function of incidence angle. The rotation axis of the specimens was aligned parallel with the hairs. The specimens were carefully prepared by removing all internal organs and thus leaving only the cuticle with the hair cover for measurement. Instead of using a spectrometer to obtain detailed wavelength information, a Si and an InGaAs detector were used to collect the integrated reflectivity over the wavelength range of 0.35 to 1.1μm and 0.8 to 1.7μm, respectively. The averaged values of the two detectors were then used to show the reflectivity as a function of incidence angle integrated over the entire visible and NIR spectrum (Fig. 2B). The integrated reflectivity took into account the spectral detection sensitivity of the two detectors.

3.4 Reflectivity measurement setup in the mid-infrared

A Fourier transform infrared (FTIR) spectrometer (Bruker vertex 70v) and a mid-infrared (MIR) microscope (Bruker Hyperion 1000) were used to take the MIR spectra shown in Fig. 2E. The microscope system operated in either spectroscopy mode or imaging mode, and is controlled by an internal beam splitter/mirror assembly. A set of variable metal apertures placed at the imaging plane of the microscope was used to control the collection area. Because the reflective objective of the microscope has a limited numerical aperture (NA=0.4), only a fraction of the diffuse reflection was captured. Therefore, the MIR spectra in Fig. 2E have an arbitrary unit and the values cannot be regarded as absolute reflectivity.

4. Thermodynamics measurement setup

In the thermodynamic measurements, all radiative heat transfer effects, which silver ants experience in their natural foraging environment, were mimicked. A high power Xenon lamp (Thorlabs HPLS-30-04) was used to simulate solar radiation, creating a spatially uniform power distribution at the ant specimens' surface (~1000 W m^{-2}). The radiation spectrum of the lamp matches well with the solar spectrum. A large thermoelectrically cooled metal plate (TE Technology CP-200), maintained at 5°C and coated with a high-emissivity paint, was used to simulate background radiation of a clear sky. The specimens (head or gaster of silver ants) were suspended on a specimen holder made of two pairs of thin human hairs to minimize thermal conduction. Figure S2 shows how an ant head is placed on the hairs and the experimental setup.

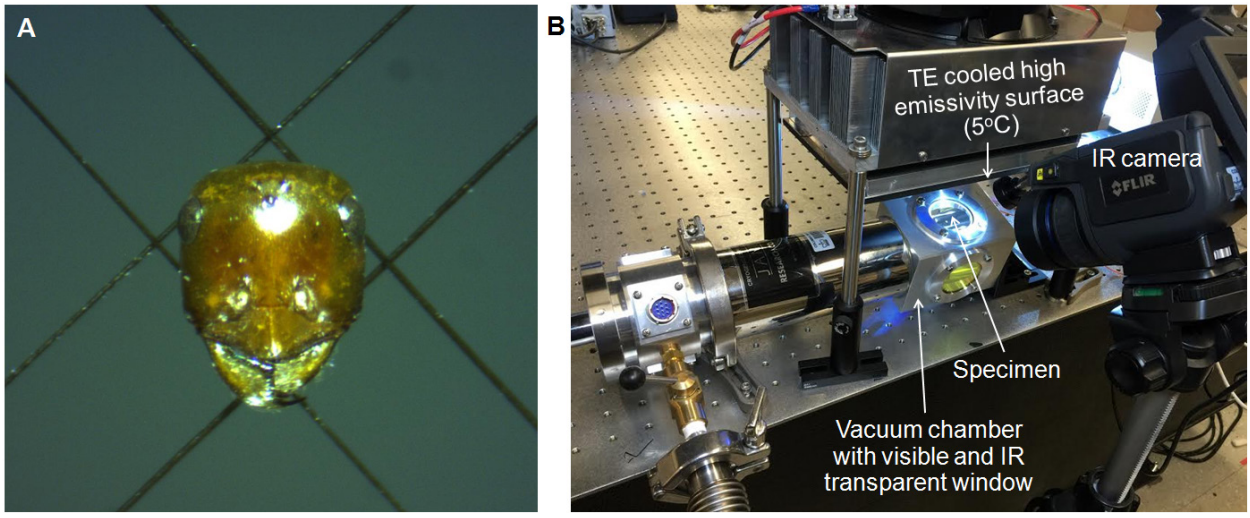

Fig. S2 Photos of specimen and experimental setup. (a) Photo of an ant head with hairs removed placed on two pairs of thin hairs. (b) Photo of the thermodynamic experimental setup.

Thermodynamics measurements were conducted both in still air and in a vacuum chamber (Janis ST-100). The vacuum experiments were conducted at pressure below 0.001 Pa to minimize convective heat transfer. The experiments enabled us to study pure thermal radiative effects so that the MIR emissivity before and after hair removal of silver ants can be extracted. The experiments in still air allowed us to study the comparative contribution of thermal radiation and natural convection in cooling the ant body.

The rise and fall of body temperature of the ant specimens was recorded at 30 frames per second with a thermal imaging camera (FLIR T640). The camera was equipped with an infrared macro lens to be able to capture detailed images of the ant body at close distances. The radiation source was turned on and off at 45-75 second intervals during recording, in order to obtain a specimen's temporal temperature profile, from which the rise and decay time constants and the steady-state temperature reached with the radiation source turned on the could be determined.

5. Wetting and drying experiment

The specimens were put through a series of wetting and drying cycles to demonstrate how the reflectivity was affected by having an index matching fluid, which filled all the gaps between the hairs and the cuticle. A solution of 70% ethanol and 30% water was used as the emersion fluid, and the reflectivity was characterized through a series of optical images taken with the dark field mode of an optical microscope (Zeiss Axio Imager). The wetting and drying cycle experiment (Fig. S3) shows that the enhancement in reflectivity is greatly suppressed when the hairs are completely immersed in the ethanol-water solution, which destroys both Mie scattering within the hairs and total internal reflection at the bottom facets of the hairs. As the solution evaporated, individual hairs started to light up, until all the hairs became bright, when the solution had completely evaporated (see supplementary movie S1).

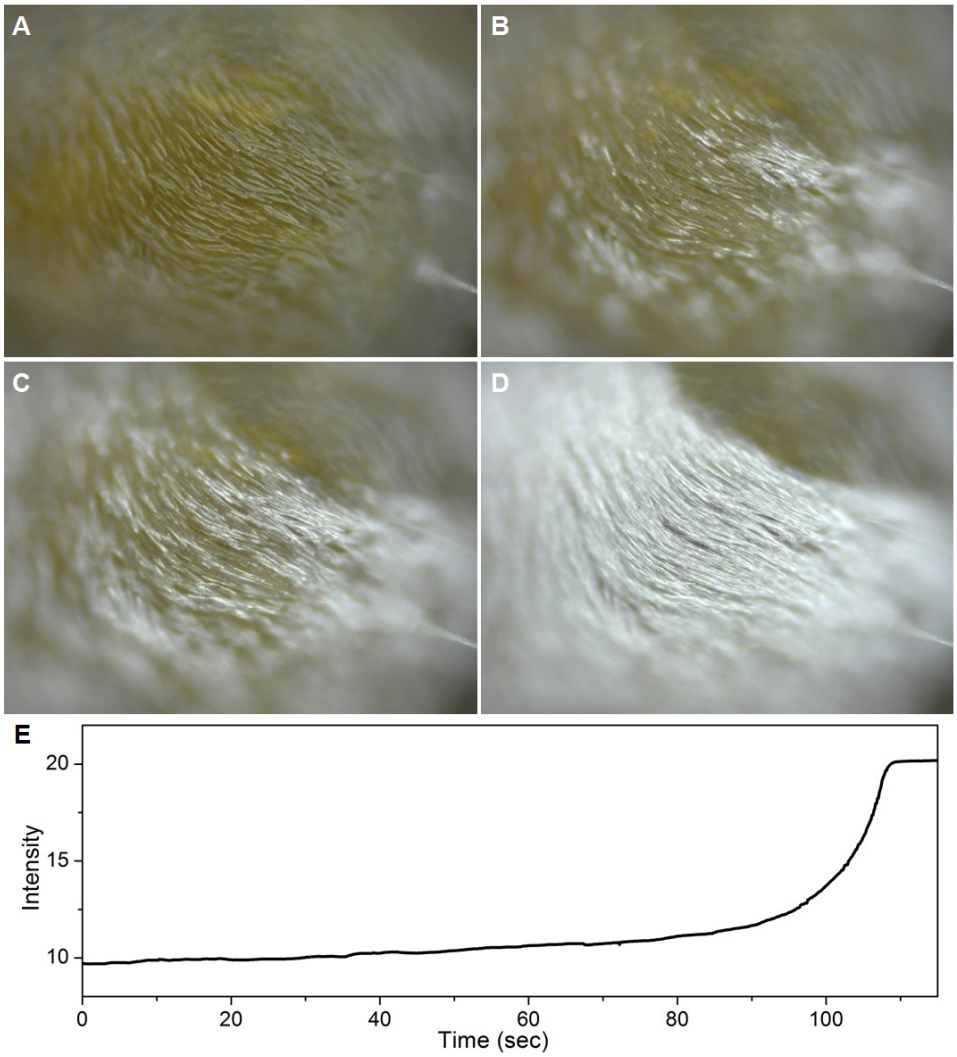

Fig. S3 Wetting and drying experiment. Optical images taken during the drying cycle of the wetting and drying experiment at (**A**) 10, (**B**) 100, (**C**) 105 and (**D**) 112 seconds after the drying process started. (**E**) Intensity of reflected visible light as a function of time during the drying process.

6. Hair distribution

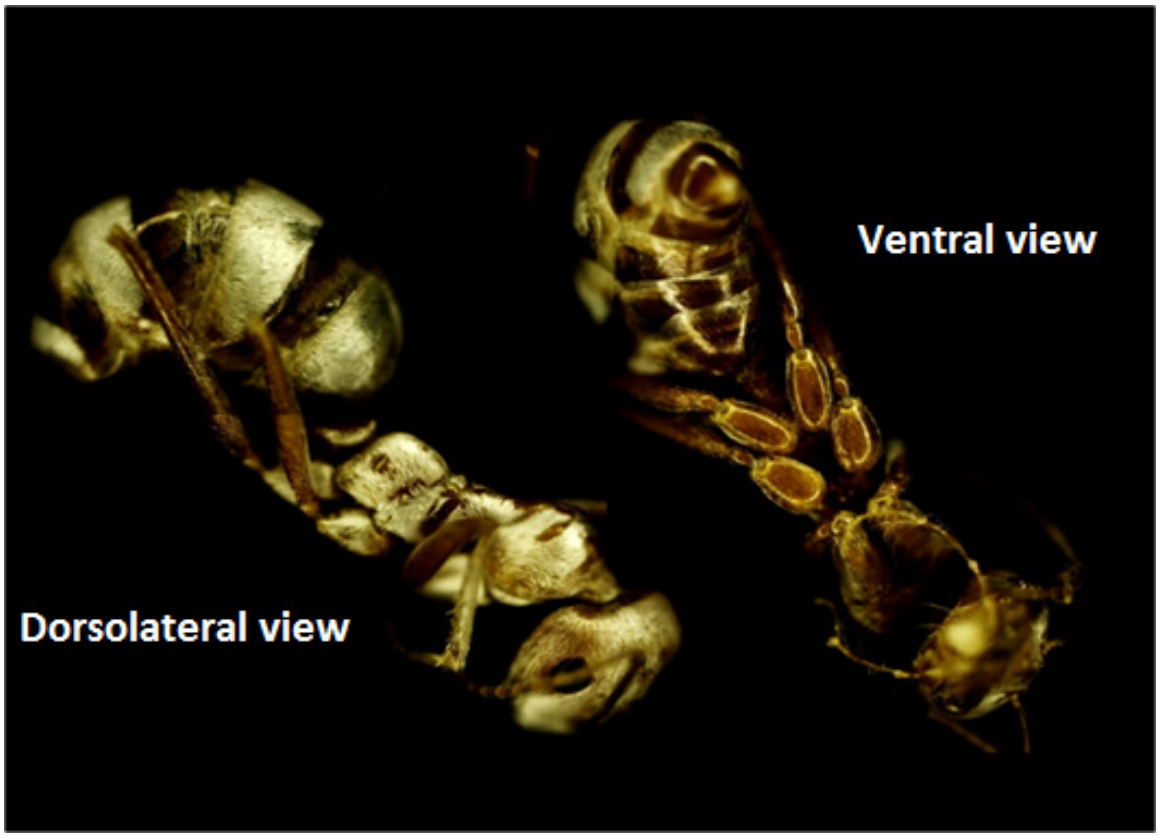

Fig. S4 Dorsolateral and ventral view of a silver ant as seen in the dark field mode of the optical microscope. The figure shows that the hairs cover only the dorsolateral sides of the ant's body, leaving the ventral side freely exposed to the desert floor.

7. Finite-difference time-domain simulations

The finite-difference time-domain (FDTD) method was used to simulate reflectivity as a function of both wavelength and angle of incidence. Specifically, we recreated the microstructural details of the hair cover in computer models (cuticle is represented by a semi-infinite substrate), assigned realistic optical properties of the chitin-protein complex (refractive index ~ 1.56, obtained from spectroscopic measurements) to the microstructures, and conducted full-wave simulations to study the interaction between light and the cuticular structures. The geometries and relative positions of the hairs were randomized so as to mimic the ant's actual pubescence (hair cover, see Fig. 1D).

Supplementary Text

1. Triangular dielectric resonator and Mie resonance

1.1. Mie resonances in single triangular hairs

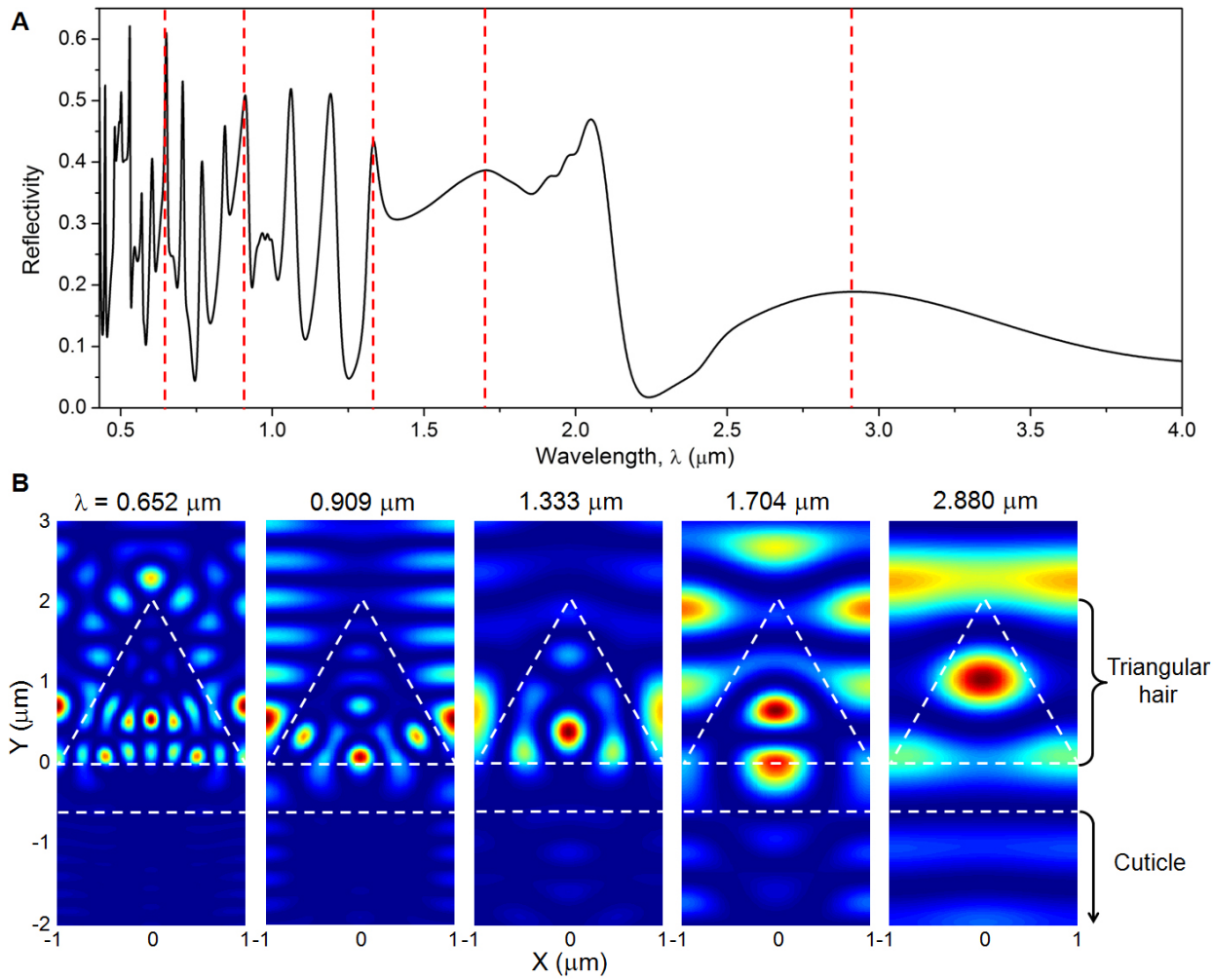

Fig. S5 Mie resonances in triangular hairs. (**A**) Reflectivity spectrum for a periodic array of triangular hairs with TE polarized incident light. Peaks in the spectra are due to Mie resonances in the triangular hairs. Reflectivity is substantially enhanced at these resonances. Vertical dashed lines indicate a few positions on the spectrum where enhanced reflectivity occurs due to Mie resonances. The corresponding distributions of light intensity at these wavelengths are plotted in (**B**). (**B**) Cross-sectional view of two-dimensional distribution of light intensity (square of the absolute value of the electric field component of light, or |Electric field|^2) for five exemplary Mie resonances. The reflectivity peak at λ=2.880 μm is the fundamental TE Mie resonance. The peaks at shorter wavelengths represent higher-order Mie resonances in the triangular hair. In this FDTD simulation both the height and the width of the triangular hair are set to 2 μm. The gap between the bottom facet of the triangular hair and the surface of the cuticle is 600 nm. As the size of the hair varies, the Mie resonance modes of the triangular hairs will shift as well: increases and decreases of widths and heights will lead to red-shifts and blue-shifts, respectively.

1.2 Effects of the gap between the bottom hair facet and the cuticular surface

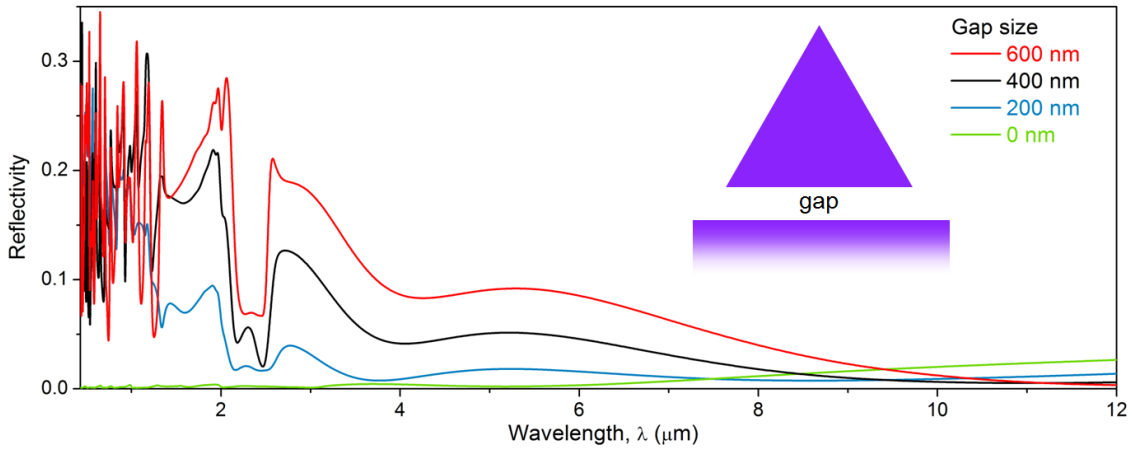

Fig. S6 Spectra of reflectivity as a function of the gap size for a periodic array of triangular hairs. Reflectivity in the visible and NIR increases as the gap opens up. Physically, the near-field coupling between triangular hairs and the substrate (cuticle) reduces the strength of Mie resonance. This near-field coupling effect becomes weaker as the gap size increases. Reflectivity is very small when the hairs are in contact with the cuticular surface (i.e., gap size = 0). The averaged reflectivity spectra under TE and TM polarized incident light were plotted (for definition of TE and TM, see Fig. S1).

2. Coupled triangular dielectric resonators and randomized hair structure

2.1 Simulation of randomized hair structure

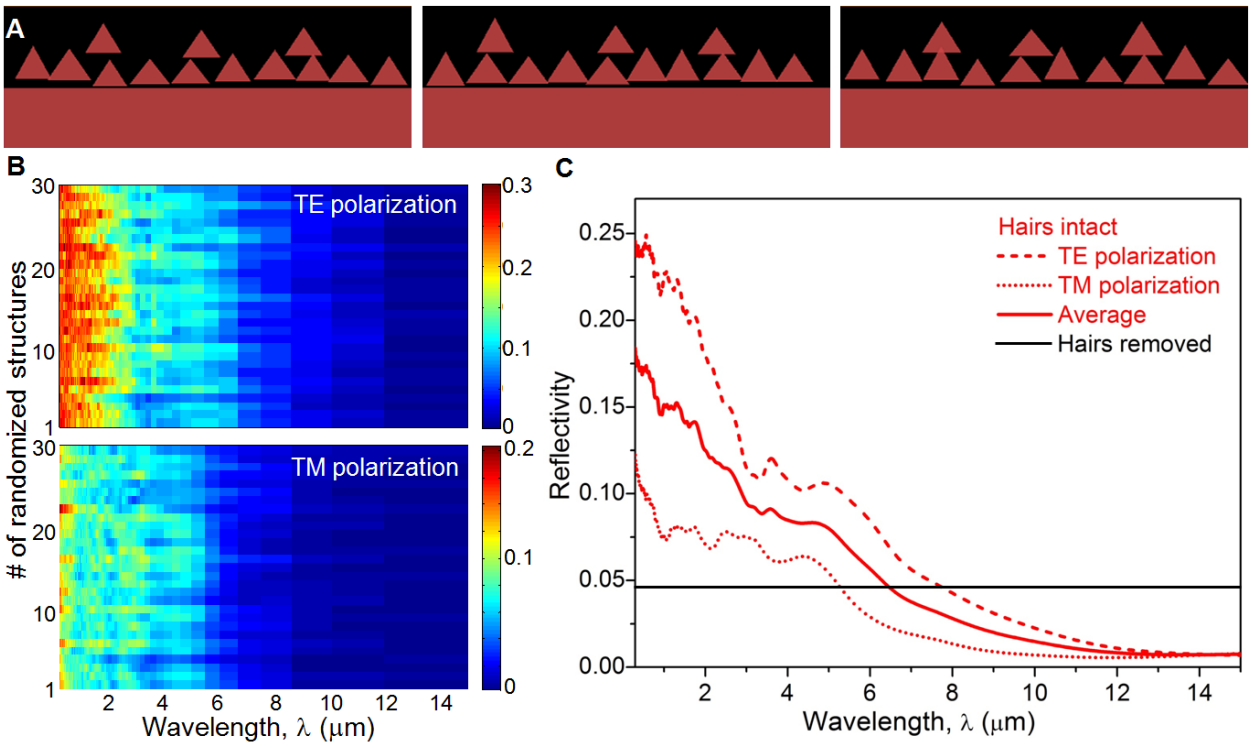

Fig. S7 Simulation of randomized hair structure. (**A**) Three exemplary arrangements of the triangular hairs. (**B**) Simulated reflectivity as a function of wavelength at normal incidence for 30

different random arrangements of the hair structure. (**C**) Reflectivity spectra averaged over 30 simulations. The reference is for an infinitely thick chitin-protein complex layer with refractive index n=1.56. The spectra show a significant enhancement of reflectivity in the visible and NIR and a decrease of reflectivity (or increase of emissivity) in the MIR. The layered structure and the coupling of modes between neighboring hairs lead to a broadening of the Mie resonance modes. Simulated reflectivity from TE polarized light is higher when compared to TM polarized light. This simulated birefringent effect from the hair array agrees with the measured results (Fig. S1),

2.2 Comparison between triangular and circular hairs of the same cross-sectional area

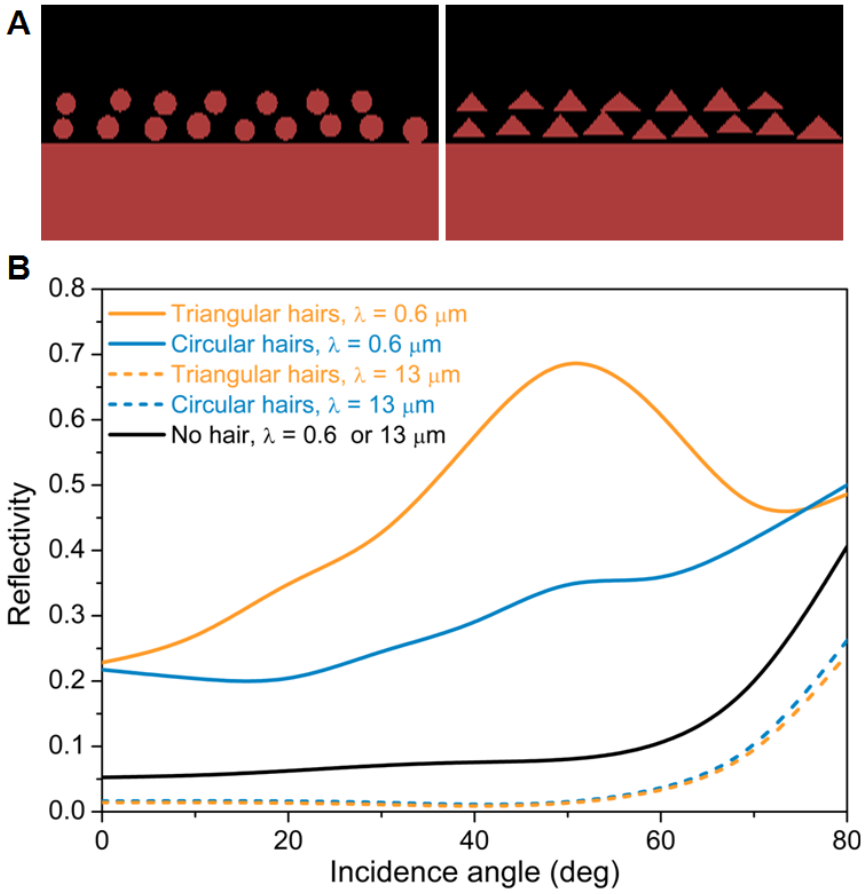

Fig. S8 Comparison between triangular and circular hairs. (**A**) Hair arrays with circular and triangular cross-sections used in the FDTD simulations. The locations and the cross-sectional dimensions of the hairs are randomized (cross-sectional area of corresponding triangular and circular hairs kept the same), in order to closely mimic the ant's actual structural conditions. (**B**) Simulated reflectivity spectra for unpolarized incident light at λ = 600 nm and 13 μm. In the visible (representative wavelength: λ = 600 nm), the reflectivity of triangular hairs is uniformly and significantly higher than that of circular hairs across the entire range of incidence angles (shown also in Fig. 2C). In the MIR (representative wavelength: λ = 13 μm), triangular and circular hairs have comparable values of reflectivity, because the hair cover functions as a layer

of thin film with effective optical refractive index, n_{eff}, determined by the material filling factor (percentage of space filled with the chitin-protein complex), which is the same for triangular and circular hairs. The MIR reflectivity of the hair cover is much smaller than that of the cuticle itself (black curve), because the hair cover with effective optical refractive index satisfying $1 < n_{eff} < n_{chitin}$ functions as an antireflective coating.

3. Effective medium theory

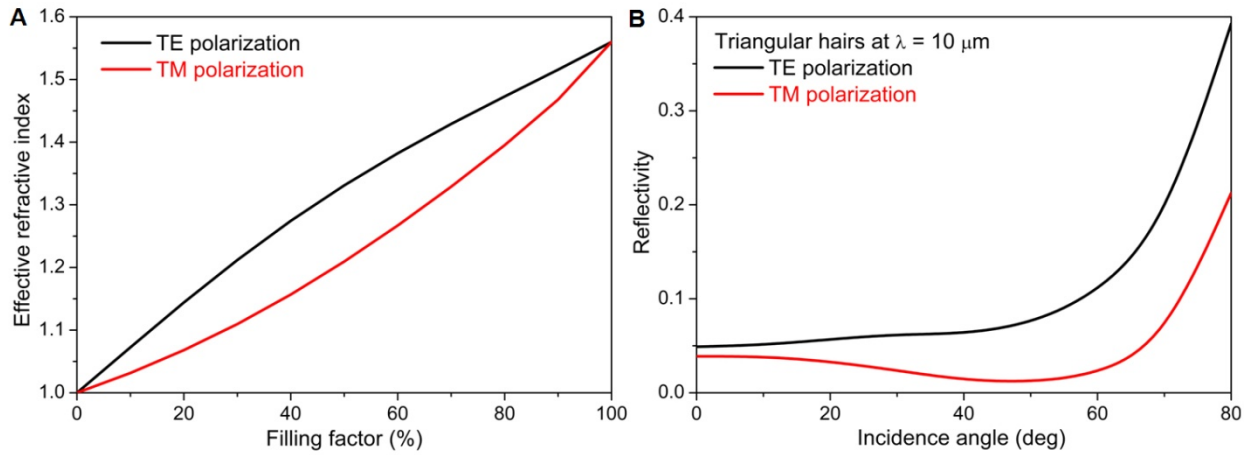

Fig. S9 Effective medium theory. (**A**) Theoretically calculated effective refractive index of a layer of triangular hairs as a function of the filling factor (percentage of space filled with the chitin-protein complex). Zero filling factor represents the apexes of the triangles, where the effective refractive index $n_{eff} = 1.0$ is matched with that of free space. Filling factor of 100% corresponds to the cuticular surface (refractive index of cuticle: 1.56; we here assume that there is no gap between triangular hairs and the cuticle). (**B**) Simulated reflectivity spectra of arrays of triangular hairs at $\lambda = 10$ μm for TE and TM polarizations. Reflectivity is uniformly lower (i.e., emissivity uniformly higher) for TM polarization. For definition of TE and TM, see Fig. S1.

As the MIR wavelength is only a few times larger than the triangular structures, a second-order approximation of the effective medium theory was used to calculate the effective refractive index of a given filling factor. The corresponding equations used to calculate the data shown in Fig. S9(A) are (*24*):

Zeroth-order approximation:

$$\varepsilon_{TE}^{(0)}(z) = f(z)\varepsilon_s + (1-f(z))\varepsilon_i \ ,$$

$$\frac{1}{\varepsilon_{TM}^{(0)}(z)} = \frac{f(z)}{\varepsilon_s} + \frac{(1-f(z))}{\varepsilon_i} \ , \qquad (2)$$

Second-order approximation:

$$\varepsilon_{TE}^{(2)}(\mathrm{z}) = \varepsilon_{TE}^{(0)}(z)\left[1+\frac{\pi^2}{3}\left(\frac{\Lambda}{\lambda}\right)^2 f^2(\mathrm{z})[1-f(\mathrm{z})]^2 \frac{(\varepsilon_s-\varepsilon_i)^2}{\varepsilon_0 \varepsilon_{TE}^{(2)}(z)}\right]$$
$$\varepsilon_{TM}^{(2)}(z) = \varepsilon_{TM}^{(0)}(z)\left[1+\frac{\pi^2}{3}\left(\frac{\Lambda}{\lambda}\right)^2 f^2(\mathrm{z})[1-f(\mathrm{z})]^2 (\varepsilon_s-\varepsilon_i)^2 \frac{\varepsilon_{TE}^{(2)}}{\varepsilon_0}\left(\frac{\varepsilon_{TM}^{(0)}(z)}{\varepsilon_i \varepsilon_s}\right)^2\right], \quad (3)$$

The equation set (2) corresponds to the zeroth-order approximation of the effective permittivity for TE (aligned parallel with hairs) and TM (perpendicular to hairs) incident light. Here *f* is the filling factor at a given layer of the effective medium marked by its z position. Λ is the width of the triangular hair cross section, ε_s and ε_i are the permittivity of the hair and air, respectively, and λ is the MIR wavelength of interest. This estimation is accurate only when wavelength is much larger than the structure. When wavelength is only a few times larger than the structure, as is the case with triangular hairs responding to MIR radiation, the second-order approximation is used, as shown above in equation set (3).

4. Heat transfer model

The temporal temperature profile of the ants in their natural environment can be described by the following equation (*25*):

$$C\frac{dT}{dt} = \alpha' Ps - \varepsilon\sigma T^4 s' + \alpha\sigma T_s^4 s + \alpha'' \sigma T_g^4 s - hs'\left(T - T_a\right) \quad (4)$$

CdT/dt describes the overall rate of change in stored thermal energy. The thermal capacity $C = cw$, where c, the specific heat for chitin, is 1.56 $Jg^{-1}K^{-1}$ (*26*) and w is the weight of the specimen.

α'Ps is the absorbed power of the light source (the Sun, or the Xenon lamp in the thermodynamic measurements); α' is the absorptivity averaged over the spectrum of the light source; P is the light intensity (power per unit area) incident onto the specimen; and s is the specimen area that intersects the incoming light beam (projected area).

εσT⁴s' is the thermal radiation from the ant specimen to the surrounding environment, hence its negative sign; ε is the emissivity averaged over the entire surface of the silver ants (i.e., both hairy and bald regions) and averaged over the spectrum of a blackbody at temperature T; σ is the Stefan-Boltzmann constant 5.67×10^{-8} $Wm^{-2}K^{-4}$; and s' is the surface area of the specimen.

ασT_s^4s is the absorption of blackbody radiation from the sky; α is ant absorptivity averaged over the spectrum of a blackbody at temperature T_s, which is the radiative temperature of the sky (*10*).

α"σT_g^4s is the absorption of blackbody radiation from the desert floor; α'' is ant absorptivity averaged over the spectrum of a blackbody at temperature T_g, which is the temperature of the surface of the desert sand.

hs'(T-T$_a$) is the power transferred through thermal convection; *h* is heat transfer coefficient; and T_a is the temperature of air surrounding the ant.

Note that α and α'' have different values, as the absorptivity of the hairy top and lateral sides of the ant's body differs from that of the bald ventral body surface. In addition, we assume that there is minimal heat transfer through conduction, as the thin long legs of these desert ants minimize thermal conduction from the desert floor (*27*).

In order to obtain an analytical solution from equation (4), the thermal radiation term $\varepsilon\sigma T^4 s'$ can be linearized in the following way:

$$\begin{aligned}\varepsilon\sigma T^4 s' &= \varepsilon\sigma s'\left(T_{avg}+T-T_{avg}\right)^4 = \varepsilon\sigma s'\mathrm{T}_{avg}{}^4\left(1+\frac{T-T_{avg}}{T_{avg}}\right)^4 \\ &\approx \varepsilon\sigma s' T_{avg}{}^4\left(1+4\frac{T-T_{avg}}{T_{avg}}\right) = \varepsilon\sigma s' T_{avg}{}^4 + 4\varepsilon\sigma s' T_{avg}{}^3\left(T-T_{avg}\right) = 4\varepsilon\sigma s' T_{avg}{}^3 T - 3\varepsilon\sigma s' T_{avg}{}^4\end{aligned} \tag{5}$$

Equation (4) can then be simplified to:

$$C\frac{dT}{dt} = -\left(4\varepsilon\sigma s' T_{avg}{}^3 + hs'\right)T + \left(3\varepsilon\sigma s' T_{avg}{}^4 + \alpha' Ps + \alpha\sigma T_s^4 s + \alpha''\sigma T_g^4 s + hs' T_a\right) \equiv -BT + A \tag{6}$$

where B = $\left(4\varepsilon\sigma s' T_{avg}{}^3 + hs'\right)$ and A = $\left(3\varepsilon\sigma s' T_{avg}{}^4 + \alpha' Ps + \alpha\sigma T_s^4 s + \alpha''\sigma T_g^4 s + hs' T_a\right)$

Solving the ordinary differential equation (6), the temperature T of the ant specimen can be expressed as

$$T \propto \pm\exp\left(-\frac{B}{C}t\right) \tag{7}$$

where

$$\tau_r = \tau_d = \frac{C}{B} = \frac{C}{4\varepsilon\sigma s' T_{avg}{}^3 + hs'} \qquad \text{(in air)} \tag{8}$$

is the rise and decay time constant characterizing the specimen's temperature change. This equation shows that the time constants are proportional to the thermal capacity, *C*, of the specimen, and inversely proportional to the sum of radiative and convective heat transfer rates. The equation also shows that the rise and decay time are identical.

For thermodynamic measurements performed in vacuum, the equation can be further simplified by taking out the effect of convective heat transfer, so that the parameter *h* can be set to zero. The rise and decay time constants can then be expressed as

$$\tau_r = \tau_d = \frac{C}{4\varepsilon\sigma s' T_{avg}^{\ 3}} \qquad \text{(in vacuum)} \qquad (9)$$

The ant reaches its steady-state body temperature when dT/dt is equal to zero, i.e., when there is no net heat transfer into or out of the ant's body. For vacuum experiments without convective heat transfer, the resulting relationship is:

$$\varepsilon\sigma T^4 s' = \alpha' P s + \alpha\sigma T_s^4 s + \alpha'' \sigma T_g^4 s \qquad \text{(in vacuum)} \qquad (10)$$

with the steady-state temperature:

$$\mathrm{T} = [\frac{1}{\varepsilon\sigma s'}(\alpha' P s + \alpha\sigma T_s^4 s + \alpha'' \sigma T_g^4 s)]^{1/4} \approx \left(\frac{\alpha' P s}{\varepsilon\sigma s'}\right)^{1/4} \qquad \text{(in vacuum)} \qquad (11)$$

When blackbody radiation from the sky and the desert floor are small as compared to the radiation from the sun or Xenon lamp (as it has been the case in the thermodynamic measurements), the steady-state temperature is proportional to *α'*, i.e., the absorptivity of the ant's body averaged over the solar spectrum, and inversely proportional to *ε,* i.e., the emissivity of the ant's body in the mid-infrared.

In the presence of convection and at thermal steady-state, according to equation (4), we have

$$\alpha' P s - \varepsilon\sigma T^4 s' + \alpha\sigma T_s^4 s + \alpha'' \sigma T_g^4 s - h s' \left(T - T_a\right) = 0 \qquad \text{(in air)} \qquad (12)$$

The steady-state temperature *T* can be obtained by numerically solving the above equation.

5. Extracting MIR emissivity and convective heat transfer coefficient from thermodynamic experiment data

Thermodynamic experiments were conducted using the gaster and head parts of silver ants. Temporal temperature profiles were taken before and after hair removal in vacuum and in still air. The experiments conducted in vacuum allowed us to exclude conductive and convective thermal transfer effects, so that we can study the sole effect of radiative heat transfer and extract the MIR emissivity before and after hair removal. The experiments conducted in still air allowed us to study the comparative contributions of radiative cooling and natural convection, and extract convective heat transfer coefficient *h* with and without hair cover. According to equations (8) and (9), we have

$$\begin{aligned} \tau_{vac,hair} &= \frac{m_{hair} c}{4\bar{\varepsilon}_{hair}\sigma s' \bar{T}_{vac,hair}^{\ 3}}, \quad \tau_{vac,bald} = \frac{m_{bald} c}{4\varepsilon_{bald}\sigma s' \bar{T}_{vac,bald}^{\ 3}} \\ \tau_{air,hair} &= \frac{m_{hair} c}{4\bar{\varepsilon}_{hair}\sigma s' \bar{T}_{air,hair}^{\ 3} + h_{hair} s'}, \quad \tau_{air,bald} = \frac{m_{bald} c}{4\varepsilon_{bald}\sigma s' \bar{T}_{air,bald}^{\ 3} + h_{bald} s'} \end{aligned} \qquad (13)$$

These four equations allow us to solve for MIR emissivities, $\bar{\varepsilon}_{hair}$ and ε_{bald}, and convective heat transfer coefficients, h_{hair} and h_{bald}, before and after hair removal. The results for the gaster and head parts of silver ants are summarized in the following table:

Table S1

Specimens	Gaster		Head	
Conditions	Before hair removal	After hair removal	Before hair removal	After hair removal
Mass	0.4774mg	0.4729mg	m_{hair}=0.4836mg	m_{bald}=0.4801mg
Surface area	s' =25.93 mm^2		s' =20.86 mm^2	
Time constant of temperature change in vacuum	$\tau_{vac,hair}$ = 4.627 sec	$\tau_{vac,bald}$ = 4.937 sec	$\tau_{vac,hair}$ = 5.947 sec	$\tau_{vac,bald}$ = 6.126 sec
Time constant of temperature change in air	$\tau_{air,hair}$ = 1.445 sec	$\tau_{air,bald}$ = 1.408 sec	$\tau_{air,hair}$ = 1.713 sec	$\tau_{air,bald}$ = 1.688 sec
Average temperature during thermodynamic experiment in vacuum	$\bar{T}_{vac,hair}$ = (T_{max}+T_{min})/2= (50.28°C +30.27°C) = 40.28°C	$\bar{T}_{vac,bald}$ = (T_{max}+T_{min})/2= (56.16°C +30.43°C) = 43.30°C	$\bar{T}_{vac,hair}$ = 41.66°C (T_{max}+T_{min})/2= (51.42°C +30.43°C) = 41.66°C	$\bar{T}_{vac,bald}$ = 45.36°C (T_{max}+T_{min})/2= (60.56°C +32.16°C) = 45.36°C
Average temperature during thermodynamic experiment in air	$\bar{T}_{air,hair}$ = (T_{max}+T_{min})/2= (43.50°C +29.74°C) = 36.62°C	$\bar{T}_{air,bald}$ = (T_{max}+T_{min})/2= (46.61°C +29.98°C) = 38.30°C	$\bar{T}_{air,hair}$ = 37.54°C (T_{max}+T_{min})/2= (44.29°C +30.78°C) = 37.54°C	$\bar{T}_{air,bald}$ = 39.47°C (T_{max}+T_{min})/2= (47.45°C +31.49°C) = 39.47°C
Average mid-infrared emissivity	$\bar{\varepsilon}_{hair}$ = 0.89	ε_{bald} = 0.80	$\bar{\varepsilon}_{hair}$ = 0.86	ε_{bald} = 0.80
Convective heat transfer coefficient	h_{hair} = 13.5 W/m^2/K	h_{bald} = 14.4 W/m^2/K	h_{hair} = 15.3 W/m^2/K	h_{bald} = 15.7 W/m^2/K

The MIR emissivity extracted in the above table is the effective emissivity averaged over the entire surface of the specimen, including both hair-covered regions and naturally bald regions. The average emissivity of the gaster decreases from $\bar{\varepsilon}_{hair} = 0.89$ to $\varepsilon_{bald} = 0.80$ with hairs removed. Considering that the hairs cover approximately 75% of the gaster (dorsal and lateral regions), we have $\bar{\varepsilon}_{hair} = 75\%\varepsilon_{hair} + 25\%\varepsilon_{bald}$. Therefore, we derive that the emissivity of the hair-covered region is $\varepsilon_{hair} = 0.92$, and that the hair cover enhances the MIR emissivity by (0.92-0.8)/0.8=15%.

Similarly, the average emissivity of the silver ant head decreases from $\bar{\varepsilon}_{hair} = 0.86$ to $\varepsilon_{bald} = 0.80$ with hair removal. Considering that the hairs cover only about 50% of the head (dorsal side), we have $\bar{\varepsilon}_{hair} = 50\%\varepsilon_{hair} + 50\%\varepsilon_{bald}$. Therefore, we derive that the emissivity of the hair-covered region to be $\varepsilon_{hair} = 0.92$, which agrees perfectly with the value obtained from the gaster.

The extracted convective heat transfer coefficient, h, increases slightly with hair removal, from h_{hair} = 13.5 W/m^2/K to h_{bald} = 14.4 W/m^2/K for the gaster, and from h_{hair} = 15.3 W/m^2/K to h_{bald} = 15.7 W/m^2/K for the head. The slightly smaller heat transfer coefficient of natural convection with hair cover is because the stagnant air between the hair cover and the cuticle creates a resistance to convective heat transfer from inside the ant body.

The extracted convective heat transfer coefficient, h, agrees reasonably well with the value h = 12.7 W/m^2/K calculated using the following equations (*28*)(*29*):

$$\begin{aligned} Nu_D &= 0.474 Ra_D^{1/4} = \frac{hD}{k} \\ Ra_D &= Gr_D Pr \\ Pr &= 0.711 \\ Gr_D &= \frac{g\beta \Delta T D^3}{\nu^2} \end{aligned} \tag{14}$$

where Nu_D, Ra_D, and Gr_D are, respectively, the averaged Nusselt number, the Rayleigh number, and the Grashof number of characteristic length D. Pr = 0.711 is the Prandtl number of air at 40^{o}C. g=9.81 m/s^2 is the acceleration of gravity, β=1/313 1/K is the thermal expansion coefficient of air at 40^{o}C, ΔT=15K (temperature difference between specimen and surrounding air at thermal steady-state), D~1.2 mm is the diameter of the specimen, ν = 16.97×10^{-6} m^2/s is the kinematic viscosity of air at 40^{o}C, and k=0.0271 W/m/K is the thermal conductivity of air at 40^{o}C.

6. Solving steady-state temperature using heat transfer model

Using parameters extracted from experiments, we can numerically solve equation (12) to obtain steady-state temperature, and study the comparative contributions of enhanced visible and NIR reflectivity and enhanced MIR emissivity in reducing the steady-state temperature under different convective heat transfer conditions.

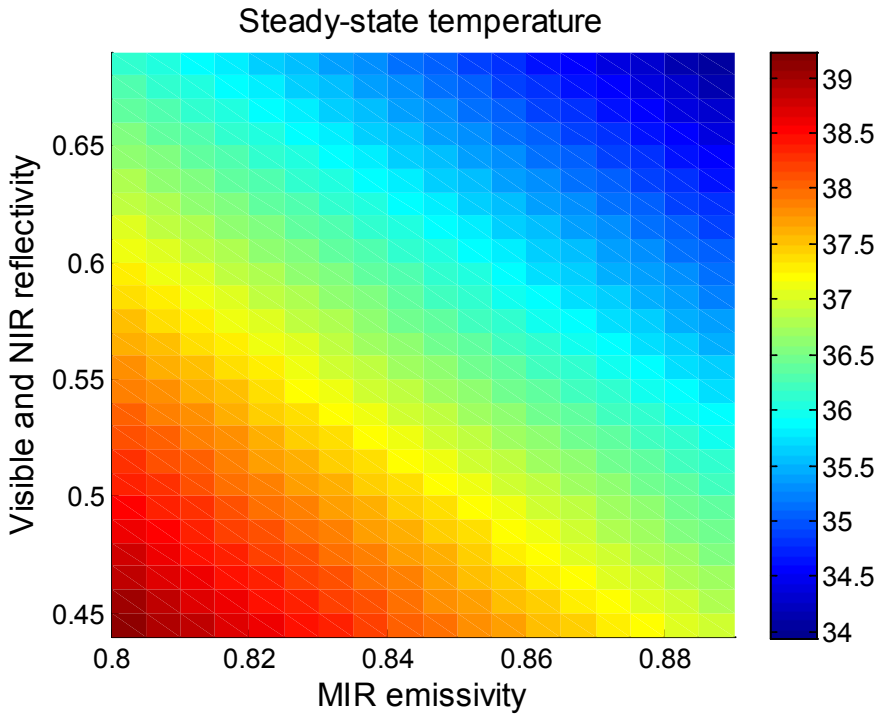

Fig. S10 Steady-state temperature calculated using heat transfer model. Steady-state temperature as a function of visible and NIR reflectivity $R_{VIS\text{-}NIR}$ and MIR emissivity ε_{MIR} at h=15 W/m^2/K (natural convection).

Figure S10 shows the steady-state temperature as a function of visible and NIR reflectivity $R_{VIS\text{-}NIR}$ and MIR emissivity ε_{MIR} in the presence of natural convection. $R_{VIS\text{-}NIR}$ ranges from 0.44 to 0.69 (or absorptivity $\alpha_{VIS\text{-}NIR}$ ranges from 0.31 (with hairs) to 0.56 (hairs removed)), and ε_{MIR} from 0.8 to 0.89. The way we determined the variation ranges of $R_{VIS\text{-}NIR}$ and ε_{MIR} is described in the subsequent section. Removing hairs from specimens decreases $R_{VIS\text{-}NIR}$ from 0.69 to 0.44 and ε_{MIR} from 0.89 to 0.80. As a result, the steady-state temperature increases from ~34^{o}C to ~39.2^{o}C (i.e., from the upper right corner to the lower left corner in Fig. S10). The effects of $R_{VIS\text{-}NIR}$ and ε_{MIR} are quite comparable, as the temperature gradient in Fig. S10 is essentially diagonal. If $R_{VIS\text{-}NIR}$ and ε_{MIR} were not correlated and were able to change independently: (a) when ε_{MIR} increases from 0.8 to 0.89 for fixed $R_{VIS\text{-}NIR}$, steady-state temperature decreases by ~2^{o}C, (b) when $R_{VIS\text{-}NIR}$ increases from 0.44 to 0.69 for fixed ε_{MIR}, steady-state temperature decreases by ~3^{o}C.

Figure S11 shows the steady-state temperature with and without hair cover and the decrease in steady-state temperature caused by the hair cover as a function of the convective heat transfer coefficient, h. The latter scales as the square root of wind speed. At a high wind speed, convection dominates over radiative heat dissipation and solely balances the energy input due to solar radiation. Under this condition, the presence of the hair cover, or enhancement of $R_{VIS\text{-}NIR}$ and ε_{MIR}, is unimportant, because the steady-state temperature will be close to the air temperature. However, foraging activities of silver ants regularly occur under low wind or even still air

conditions, during which the ants have to resort to respite behavior and have thus to rely on both enhanced $R_{VIS\text{-}NIR}$ and ε_{MIR} to bring down the body temperature. In fact, under these conditions it is often observed that the ants when prevented from engaging into their respite routine actually die on the ground (*3*).

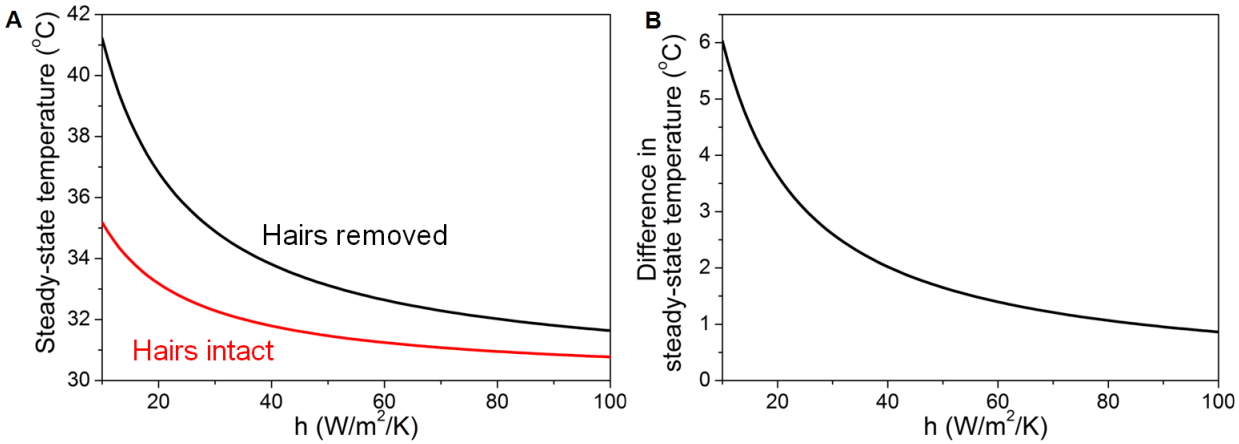

Fig. S11 Effect of hairs on steady-state temperature. (**A**) Steady-state temperature as a function of convective heat transfer coefficient, *h*, obtained by numerically solving equation (12). (**B**) Decrease in steady-state temperature caused by the hair cover as a function of *h*.

The way we calculated the variation range of $R_{VIS\text{-}NIR}$ and ε_{MIR} according to experimental results are discussed in the following. Assuming that the body parts (head or gaster) of silver ants can be approximated as a sphere with radius *r*, and that θ and φ are angles of the spherical coordinate system. The total absorbed power $\boldsymbol{\alpha' Ps}$ is calculated in the following way. The power incident onto a small area $dA=r^2 \sin\theta d\theta d\varphi$ on the sphere is $PdA\cos\theta$. Therefore the total power incident onto the upper half of the sphere is:

$$\int_{\varphi=0}^{2\pi}\int_{\theta=0}^{\pi/2}\left(P\cos\theta\right)r^2\sin\theta d\theta d\varphi = P\pi r^2 \tag{15}$$

The total reflected power from the upper half of the sphere is:

$$\int_{\varphi=0}^{2\pi}\int_{\theta=0}^{\pi/2}\left[R\left(\theta\right)P\cos\theta\right]r^2\sin\theta d\theta d\varphi \tag{16}$$

where $R(\theta)$ is angular dependent visible and NIR reflectivity. Thus, the total absorbed power is the difference of (15) and (16):

$$\begin{aligned}\alpha' Ps &= \pi r^2 P - \int_{\varphi=0}^{2\pi}\int_{\theta=0}^{\pi/2}\left[R\left(\theta\right)P\cos\theta\right]r^2\sin\theta d\theta d\varphi \\ &= \left[1-\frac{1}{\pi}\int_{\varphi=0}^{2\pi}\int_{\theta=0}^{\pi/2}R\left(\theta\right)\sin\theta\cos\theta d\theta d\varphi\right]P\left(\pi r^2\right)\end{aligned} \tag{17}$$

Therefore, the absorptivity in the visible and NIR is:

$$\alpha' = 1 - \frac{1}{\pi}\int_{\varphi=0}^{2\pi}\int_{\theta=0}^{\pi/2} R(\theta)\sin\theta\cos\theta d\theta d\varphi \tag{18}$$

The angular dependent reflectivity $R(\theta)$ is calculated in the following way. The reflectivity measured from various spots on the ant body at zero-degree angle of incidence and normalized to solar irradiance according to equation (1) is $R_{hair}(\theta=0) = 60\%\pm15\%$ for hair-covered regions and $R_{bald}(\theta=0) = 40\%\pm10\%$ for regions with hairs removed. Using the measured increase in reflectivity as a function of incidence angle, $\Delta R_{hair}(\theta)$ and $\Delta R_{bald}(\theta)$ (Fig. 2B), we can then calculate the angular dependent reflectivity:

$$\begin{aligned} R_{hair}(\theta) &= R_{hair}(\theta=0) + \Delta R_{hair}(\theta) \\ R_{bald}(\theta) &= R_{bald}(\theta=0) + \Delta R_{bald}(\theta) \end{aligned}. \tag{19}$$

Using equations (18) and (19), the visible and NIR absorptivity α' for the hair-covered regions and regions with hairs removed are, respectively,

$$\begin{aligned} \alpha'_{hair} &= 1 - \frac{1}{\pi}\int_{\varphi=0}^{2\pi}\int_{\theta=0}^{\pi/2} R_{hair}(\theta)\sin\theta\cos\theta d\theta d\varphi = 0.31 \\ \alpha'_{bald} &= 1 - \frac{1}{\pi}\int_{\varphi=0}^{2\pi}\int_{\theta=0}^{\pi/2} R_{bald}(\theta)\sin\theta\cos\theta d\theta d\varphi = 0.56 \end{aligned} \tag{20}$$

Therefore, the visible and NIR reflectivity $R_{VIS\text{-}NIR}$ for the hair-covered regions and regions with hairs removed are, respectively, 0.69 and 0.44 (i.e., the range of $R_{VIS\text{-}NIR}$ used in Fig. S10).

The MIR emissivity ε is calculated using the following equation (*8*),

$$\varepsilon = \frac{\int_{\varphi=0}^{2\pi} d\varphi \int_{\theta=0}^{\pi/2} [1 - R(\theta)]\sin\theta\cos\theta d\theta}{\int_{\varphi=0}^{2\pi} d\varphi \int_{\theta=0}^{\pi/2} \sin\theta\cos\theta d\theta} \tag{21}$$

Here $R(\theta)$, shown in Fig. 2F, is the MIR reflectivity obtained from full-wave FDTD simulations. It was averaged over TE and TM incident polarizations and over all possible orientation angles of the hair arrays (characterized by azimuthal angle from φ=0 to 90^o in step of 10^o). $R(\theta)$ is also weighted by the blackbody radiation spectrum at 50^{o}C using an equation similar to equation (1). We obtained using equation (21) that the emissivity for the bald and hairy regions, respectively, is $\varepsilon_{bald} = 0.87$ and $\varepsilon_{hair} = 0.93$. While $\varepsilon_{hair} = 0.93$ agrees well with the value extracted from the thermodynamic experiments (where we obtained $\varepsilon_{hair} = 0.92$), $\varepsilon_{bald} = 0.87$ seems to be an overestimation. $\varepsilon_{bald} = 0.87$ is obtained in FDTD simulations assuming that the sclerotinized chitinous exocuticle is a semi-infinite substrate. Our measurements indicate, however, that the heterogeneous internal structures of ant body enhance MIR reflection. For example, our MIR reflectivity measurements using an integration sphere, which captures all specular and diffuse

reflection, showed that the MIR reflectivity of bald regions at zero-degree incidence angle is ~10-20%, which is much larger than ~5%, the reflectivity at normal incidence of an interface between air and chitin with n=1.56. Enhanced MIR reflectivity leads to reduced MIR absorption or emissivity. The range of ε_{MIR} used in Fig. S10 is from $\varepsilon_{bald} = 0.80$ to $\overline{\varepsilon}_{hair} = 0.89$ (i.e., gaster with 75% of skin covered by hairs, $\varepsilon_{hair} = 0.92$, and 25% of skin naturally bald, $\varepsilon_{bald} = 0.80$) obtained from the thermodynamic experiments.

Movie S1. Video segment (41 seconds) taken during the drying cycle of the wetting and drying experiment. The timestamp corresponds to the amount of time since drying process started.

REFERENCES AND NOTES

1. R. Wehner, S. Wehner, Parallel evolution of thermophilia: daily and seasonal foraging patterns of heat-adapted desert ants: *Cataglyphis* and *Ocymyrmex* species. *Physiol. Entomol.* **36**, 271–281 (2011). doi:10.1111/j.1365-3032.2011.00795.x

2. Materials and methods are available as supplementary materials on *Science* Online.

3. R. Wehner, A. C. Marsh, S. Wehner, Desert ants on a thermal tightrope. *Nature* **357**, 586–587 (1992). doi:10.1038/357586a0

4. W. J. Gehring, R. Wehner, Heat shock protein synthesis and thermotolerance in *Cataglyphis*, an ant from the Sahara desert. *Proc. Natl. Acad. Sci. U.S.A.* **92**, 2994–2998 (1995). Medline doi:10.1073/pnas.92.7.2994

5. C. F. Bohren, D. R. Huffman, *Absorption and Scattering of Light by Small Particles* (John Wiley & Sons, 1998).

6. J. Schuller, T. Taubner, M. L. Brongersma, Optical antenna thermal emitters. *Nat. Photonics* **3**, 658–661 (2009). doi:10.1038/nphoton.2009.188

7. D. Lin, P. Fan, E. Hasman, M. L. Brongersma, Dielectric gradient metasurface optical elements. *Science* **345**, 298–302 (2014). Medline doi:10.1126/science.1253213

8. J. R. Howell, R. Siegel, M. P. Mengüç, *Thermal Radiation Heat Transfer* (CRC Press, ed. 5, 2010).

9. K. L. Coulson, *Solar and Terrestrial Radiation: Methods and Measurements* (Academic Press, 1975).

10. J. Monteith, M. Unsworth, *Principles of Environmental Physics* (Academic Press, Oxford, ed. 3, 2007).

11. C.-H. Sun, P. Jiang, B. Jiang, Broadband moth-eye antireflection coatings on silicon. *Appl. Phys. Lett.* **92**, 061112 (2008). doi:10.1063/1.2870080

12. J.-Q. Xi, M. F. Schubert, J. K. Kim, E. F. Schubert, M. Chen, S.-Y. Lin, W. Liu, J. A. Smart, *Nat. Photonics* **1**, 176 (2007).

13. M. J. Minot, Single-layer, gradient refractive index antireflection films effective from 035 to 25 μ. *J. Opt. Soc. Am.* **66**, 515 (1976). doi:10.1364/JOSA.66.000515

14. C. G. Granqvist, A. Hjortsberg, Surfaces for radiative cooling: Silicon monoxide films on aluminum. *Appl. Phys. Lett.* **36**, 139 (1980). doi:10.1063/1.91406

15. P. Berdahl, Radiative cooling with MgO and/or LiF layers. *Appl. Opt.* **23**, 370 (1984). Medline doi:10.1364/AO.23.000370

16. E. Rephaeli, A. Raman, S. Fan, Ultrabroadband photonic structures to achieve high-performance daytime radiative cooling. *Nano Lett.* **13**, 1457–1461 (2013). Medline

17. A. P. Raman, M. A. Anoma, L. Zhu, E. Rephaeli, S. Fan, Passive radiative cooling below ambient air temperature under direct sunlight. *Nature* **515**, 540–544 (2014). Medline doi:10.1038/nature13883

18. R. Wehner, *Jahrb. Akad. Wiss. Lit. Mainz* **89**, 101 (1989).

19. B. Heinrich, *The Hot-Blooded Insects: Strategies and Mechanisms of Thermoregulation* (Harvard Univ. Press, 1993).

20. G. S. Bakken, D. M. Gates, *Heat-Transfer Analysis of Animals: Some Implications for Field Ecology, Physiology, and Evolution* (Perspectives of Biophysical Ecology, Ecological Studies Volume 12, Springer, 1975), pp. 255–290.

21. A. C. Marsh, *Physiol. Zool.* **58**, 629 (1985).

22. H. Heatwole, S. Harrington, *J. Arid Environ.* **16**, 69 (1989).

23. J. M. Chalmers, P. R. Griffiths, *Handbook of Vibrational Spectroscopy* (John Wiley & Sons, 2002).

24. D. H. Raguin, G. M. Morris, Analysis of antireflection-structured surfaces with continuous one-dimensional surface profiles. *Appl. Opt.* **32**, 2582–2598 (1993). Medline doi:10.1364/AO.32.002582

25. D. M. Gates, *Biophysical Ecology* (Dover Publications, 1980).

26. R. A. A. Muzarelli, *Chitin* (Pergamon Press, 1977).

27. S. Sommer, R. Wehner, Leg allometry in ants: Extreme long-leggedness in thermophilic species. *Arthropod Struct. Dev.* **41**, 71–77 (2012). Medline doi:10.1016/j.asd.2011.08.002

28. O. G. Martynenko, P. P. Khramtsov, *Free-Convective Heat Transfer* (Springer, 2005).

29. H. J. Merk, J. A. Prins, *Appl. Sci. Res.* **A4**, 207 (1954).